Autonomous Camber Morphing of a Helicopter Rotor Blade with Temperature Change using Integrated Shape Memory Alloys

Matthew DiPalma
PhD Student

Farhan Gandhi
Redfern Professor and Director

Center for Mobility with Vertical Lift (MOVE)
Rensselaer Polytechnic Institute, Troy, NY 12180

ABSTRACT

The present study proposes and explores a new autonomous morphing concept, whereby an increase in helicopter rotor blade camber of the order of 12-13° is realized over the inboard section of the blade with increase in ambient temperature. The camber change is achieved through a proper integration of Shape Memory Alloys (SMAs) on the lower surface of the blade aft of the leading-edge spar. For a reference rotor (no-SMA) generating 21,000 lbs thrust, operation in hot conditions resulted in a 2,590lb loss in lift. When the SMA camber morphing section extends from the blade root to 50% span, the rotor recovered up to 43% of the lift loss at high temperature. If the camber-morphing section is further extended to 75% span, up to 82% of the lost lift can be recovered.

INTRODUCTION

Over the last couple of decades, the introduction of morphing in aerospace structures has been regarded as a highly effective means of achieving improved aerodynamic performance across diverse operating conditions. One commonly considered form of morphing on both fixed- and rotary-wing aircraft has been wing or rotor blade camber change. Prior studies have considered several different camber actuation methods such as the use of piezoelectric actuators (Refs. 1-6), pneumatic actuators (Ref. 7), conventional servomotors (Ref. 8), and shape memory alloys (Refs. 9-13). Regardless of the tradeoffs associated with specific actuation methods, all the actuation approaches require achieving some finite deformation in structures that are fundamentally rigid enough to withstand the aerodynamic loads, as well as centrifugal loads in the case of rotor blades. This, in turn, translates into significant actuation force and energy requirement.

In contrast, another approach to aircraft morphing has been to exploit change in operating state to realize structural shape change, without any dedicated actuation energy input. In rotary-wing aircraft, in particular, changes in rotor RPM, and the resultant changes in centrifugal forces acting on the blade, have been used in several studies to realize rotor span extension morphing (Refs. 14-15), chord extension morphing (Ref. 16), and rotor blade twist change (Refs. 17-21). Such an approach, where reconfiguration is achieved without the use of dedicated actuation energy input, can be referred to as *autonomous morphing*.

Submitted to the Vertical Flight Society 75th Annual Forum, Philadelphia, PA, USA, May 13-16, 2019

The present study proposes and explores a new autonomous morphing concept, whereby an increase in helicopter rotor blade camber is realized with increase in ambient temperature. The camber change is achieved through the integration of Shape Memory Alloys (SMAs) into the blade structure. SMAs are known to undergo a Martensite-Austenite phase transformation with temperature variation, accompanied by a large strain change. When the SMA is constrained, by attachment to a structure, for example, it exerts large forces on the structure when the temperature change triggers phase transformation. Through the SMA's proper integration into a helicopter rotor blade, this study demonstrates how camber change can be realized with change in temperature and assesses the influence of this camber change on the rotor aerodynamic performance.

CONCEPT DESCRIPTION AND ANALYSIS

Helicopter operation in very hot (desert-like) conditions can be highly problematic as the markedly reduced air density reduces the rotor's lift generation capability. While lift recovery may be possible at low to moderate gross weight by increasing rotor pitch, attempts to do so at high gross weight ("hot and heavy" conditions) render the aircraft susceptible to stall. The proposed concept is to introduce SMAs over the lower surface of the rotor blade aft of the leading edge-spar so as to increase the blade section camber when temperature elevation produces a Martensite-to-Austenite phase transformation, while reverting back to the baseline geometry when temperature reduction produces the reverse Austenite-to-Martensite phase transformation.

In the present study, this camber change is introduced over the inboard section of the blade, extending from the blade root to the junction with the non-morphing section, as shown in Fig. 1. The length of the morphing section is taken to be 25%, 50% or 75% span, starting from the blade root. At the junction with the non-morphing section, a seamless integration as well as a slit boundary is considered. In the former case, temperature increase produces a spanwise variation in camber over the morphing section, going from zero at the junction with the non-morphing section to a maximum value at the root of the blade. In the latter case, temperature increase produces a uniform camber change over the entire morphing section, much like a trailing-edge flap. The reference blade used in this study is a prismatic derivative of the UH-60A Black Hawk helicopter blade (with constant chord and zero twist), and has the SC1095 airfoil along the entire span.

A rigid leading-edge spar is assumed to extend from the nose to 26% chord. Over the morphing section, the region aft of the spar is deformable in camber. It has a relatively stiff aluminum trailing-edge cap extending from 80% chord to the trailing-edge, so the section between the end of the spar and the beginning of the trailing-edge cap (from 26% chord to 80% chord) undergoes chordwise bending as the morphing section of the blade cambers. The upper surface of this deformable region has a classical composite skin while the lower surface has the SMA skin, with a 180MPa modulus core in between. All material properties are listed in Table 1.

The SMA has to first be pre-stretched in the chordwise direction and can be attached to the lower surface of the blade over the morphing section either in the Austenite (hot) or the Martensite (cold) states. In the current simulations, the morphing section of the blade is envisioned as being built with reflex camber in its stress-free state (as depicted in Fig. 2). When the pre-strained SMA lower-skin in the Austenite phase is attached to the reflexed blade between the rear of the spar and the trailing-edge cap, and the pre-straining force is then released, the blade deforms to attain the cambered geometry depicted on Fig. 2 as "cambered hot state." When the temperature is reduced and the SMA undergoes a Martensitic phase transformation, it attains a geometry similar to the reference prismatic UH-60A blade (depicted in Fig. 2 as "uncambered cold state"). Temperature variation then results in the morphing section deforming between the reference and cambered geometries. Figure 2 depicts the case where the morphing section seamlessly integrated into the non-morphing section at the junction between the two regions. For the selected core stiffness, the magnitude of the initially built-in reflex, and the SMA lower surface skin's thickness and pre-strain are determined by trial and error such that the system transitions between the reference blade geometries and the desired camber deformation with variation in temperature corresponding to full phase transformations. It should be noted that if the pre-strained SMA was attached in the Martensitic phase, initial reflex would not be required and the SMA could be attached to the configuration corresponding to the reference blade geometry.

The structural analysis of the morphing blade section is conducted using ABAQUS 6.13 Finite Element Analysis. The region aft of the blade spar, extending from the blade root to the junction with the non-morphing section is modeled using between 30,000 and 90,000 linear hexahedral C3D8 elements (depending on the spanwise length of the morphing section considered). A sample of the finite element mesh is shown in Fig. 3. The conformable region is fixed to the rear of the rigid spar (clamped boundary conditions) while the root end is a free boundary. At the junction with the non-morphing section, either clamped or free boundary conditions are used corresponding to a seamless or slit junction, respectively. The SMA is modeled using the built-in ABAQUS Super-Elastic subroutine, which is based on the work of Auricchio and Taylor (Ref. 22). This subroutine captures the phase transformation between Austenite and detwinned Martensite. The properties for the NiTiNOL SMA sheet used in this study are taken from Ref. 23 and listed in Table 2. In the presence of aerodynamic loading (applied as a distributed pressure) and centrifugal loading (applied as a distributed body force), the ABAQUS simulation results allow an analysis of the stresses and strains in the morphing section of the blade as it undergoes temperature change and transitions between the Austenite and Martensite phases. The Martensite volume fraction is also examined.

Available SC1095 airfoil properties are used for aerodynamic analysis of the reference blade. For the morphing section, the deformed cross-section geometry from ABAQUS simulation after heating the SMA is used to define the cambered airfoil contour which is then analyzed using XFOIL 6.99 to evaluate the lift, drag and pitching moment coefficients over a range of airfoil angles of attack. Figure 4 depicts the deformed airfoil geometry with 15° camber, relative to the baseline SC1095 airfoil, and Fig. 5 shows the pressure variation for both the baseline and the cambered airfoil geometries. XFOIL evaluations of the aerodynamic coefficients are conducted at a Mach number of 0.15 (since the camber morphing section is inboard), and at a Reynolds number of 1.0×10^6. Lift and drag coefficient results, versus angle of attack, for the baseline SC1095 airfoil and for increasing levels of camber deformation are shown in Figs. 6 and 7, respectively. Similar results were obtained for pitching moment coefficients (not shown in the paper) and were used in the analysis. As expected, C_{L0} (the lift coefficient corresponding to zero angle of attack) is observed to increase in Fig. 6 for increasing values of camber. The maximum lift coefficient, C_{Lmax}, increases by 25% while the angle of attack decreases from 13° to 10°, when airfoil camber of 15° is introduced. Figure 7 shows a significant increase in drag with airfoil camber deformation. While this could lead to an increase in rotor power requirement, camber deformation could still be a plausible solution for helicopters near the stall boundary that are thrust limited but have sufficient installed power.

The influence of camber morphing on rotor performance is evaluated using the Rotorcraft Comprehensive Analysis System (RCAS) v15.09 (Ref. 24). Simulations are based on

the UH-60A Black Hawk helicopter with the prismatic rotor discussed above. The rotor radius is 8.17m, the blade chord is 0.53m, and the operational speed is 258RPM. RCAS simulations are run in hover (for the rotor only), with a 12x13 state dynamic inflow model, over a range of variation in collective pitch (zero cyclic pitch), and the rotor thrust and power is calculated. These calculations are carried out for cold and hot temperatures corresponding to the uncambered reference blade geometry and the morphed cambered geometry, respectively.

The study in the paper requires coupling between the analyses discussed above. The ABAQUS simulations produce the deformed airfoil geometries required by XFOIL for calculation of aerodynamic coefficients. These airfoil properties are utilized in RCAS for rotor performance evaluations, and the aerodynamic loads from RCAS are, in turn, applied to the ABAQUS model to calculate blade stresses and strains under combined (aerodynamic, centrifugal, and SMA-induced) loads.

RESULTS

Camber Morphing Over Inboard 25% Span, Slit Junction

In the first case analyzed, the morphing section extends over the inboard 25% span, with a slit boundary between the morphing and non-morphing sections. Figure 8 shows the morphing section in the initial stress-free state, reflexed to 8°. The SMA, in the Austenite state, is pre-strained to 6.6% strain in the chordwise direction and attached to the undersurface. This results in the morphing section deforming to the configuration marked as "hot state" with a 13° camber deformation. When the SMA temperature is reduced it undergoes an Austenite-to-Martensite phase transformation and transitions to the uncambered "cold state" shown on Fig. 8. Figure 9 shows the magnitude of the camber deformation versus ambient temperature, obtained from ABAQUS simulation results. The Austenite-to-Martensite phase transformation does not begin till the SMA temperature gets to 95°F. As the temperature reduces below 95°F the camber in the blade reduces and eventually disappears when the transformation completes around 40°F. With rise in temperature, the Martensite-to-Austenite phase transformation begins at around 60°F, but significant increase in camber is only observed at temperatures beyond 80°F. Completion of phase transformation and full 13° camber deformation is observed at 115°F.

Figure 10 shows the Martensite volume fraction over the lower surface of the blade. At low temperature the SMA is almost entirely Martensite. Conversely, at high temperature, the SMA is almost entirely Austenite. Figure 11 depicts the von Mises stresses within the SMA on the lower surface of the blade. For a slit junction with the non-morphing section, there is very little spanwise variation in the SMA stress state. In the hot state, the peak von Mises stress in the SMA occurs near the trailing-edge cap, where the highest curvature for the camber is experienced. In the cold state however, the von Mises stresses are much lower, due to the non-cambered geometric shape at this ambient temperature.

Figure 12 shows the chordwise strain on the upper surface. In the cold (uncambered) state the majority of the upper surface has a strain of around 0.7% as it deforms from the stress-free reflexed state. There is a narrow strip along the trailing-edge cap where the strain is higher (1.6%). In the hot (cambered) state, the upper surface strain increases to 3.1%. Figure 13 similarly shows the chordwise strain in the SMA along the lower surface. In the cold (uncambered) state the lower SMA skin experiences a strain of 4.5%. In the hot (cambered) state, the SMA skin strain further decreases to 0.3%

Camber Morphing Over Inboard 25% Span, Continuous Junction

The next configuration analyzed once again has the morphing section spanning the inboard 25% of the rotor blade, but is seamlessly integrated into the non-morphing section at the junction between the two regions. Figure 14 shows the morphing section in the initial stress-free state reflexed to 8° at the root of the blade, and the reflex linearly decays to flat at 25% span, where it joins the non-morphing outboard section of the blade. The SMA, in the Austenite state, is pre-strained to 6.6% strain in the chordwise direction at the blade root and decreases linearly to 4.2% at the junction with the non-morphing section, before attachment to the undersurface. This results in the morphing section deforming to the configuration marked as "hot state" with a 12° camber deformation. When the SMA temperature is reduced it undergoes an Austenite-to-Martensite phase transformation and transitions to the uncambered "cold state" shown on Fig. 14. The camber variation along the span can be seen more clearly in Fig. 15.

Figure 16 shows the magnitude of the root camber deformation versus ambient temperature, obtained from ABAQUS simulation results. The Austenite-to-Martensite phase transformation does not begin till the SMA temperature gets to 95°F. As the temperature reduces below 95°F the root camber in reduces and eventually disappears when the transformation completes around 40°F. With rise in temperature, the Martensite-to-Austenite phase transformation begins at around 60°F resulting in a steady increase in root camber up to a maximum value of 12° at 115°F when the transformation is completed.

Figure 17 shows the Martensite volume fraction in the SMA on the lower surface of the morphing section of the blade. At low temperature the SMA is almost 100% Martensite near the junction with the non-morphing section but reduces to between 50-75% at the blade root. At high temperature, the SMA continues to remain in the Martensitic phase at the junction with the non-morphing section while transforming completely to Austenite near the blade root. Unlike the slit boundary configuration in Fig. 10, the stress induced by the

boundary condition at the junction in the present case prevents transformation to Austenite in that region.

Figure 18 depicts the von Mises stresses within the SMA on the lower surface of the blade. For a continuous junction with the non-morphing section, a spanwise variation in the SMA stress state is observed. For both the hot and cold states, the SMA experiences the greatest stress concentration in the vicinity of the junction with the non-morphing section. Also, the von Mises stress throughout the majority of the morphing section inboard of the junction is greater in magnitude in the hot state (Austenite phase) than in the cold state (Martensite phase).

Figure 19 depicts the in-plane maximum principle strain along the upper surface of the morphing section. In this case, the maximum strain occurs at the blade root, where the maximum net change in camber deflection occurs. Note that the upper surface of the blade is entirely unstrained in the initial reflexed configuration, before the SMA is engaged. After the SMA is attached and in the cold state, the blade cambers downwards to equilibrate at 0° camber, and the upper skin experiences a moderate strain level, as shown in Fig. 19. When the SMA is heated the airfoil cambers further, and the strain in the upper skin increases in the vicinity of the blade root to a maximum of 4%. The strain in the upper skin is primarily chordwise over the entire morphing section.

Figure 20 depicts the in-plane maximum principle strain along the lower surface of the morphing section. The greatest in-plane strain for both the hot and the cold states occurs near the rigid boundary of the junction with the non-morphing section. The strain in this region is primarily spanwise in nature, which is a manifestation of the blending between no shape change and significant camber change. Change in chordwise strain is suppressed at the clamped boundary condition. While the strain is predominantly spanwise in the vicinity of the junction, some chordwise strain is observed near the inboard free end. In both the hot and cold states, the maximum in-plane principal strain reaches 6.4% near the junction with the non-morphing section. At the blade root end, the strain varies between 3.5% in the cold state to 0.1% in the hot state.

Rotor Performance Analysis

This section presents results of the performance analysis conducted using RCAS for a hovering rotor at 6,000 ft altitude, with morphing blade sections of various spanwise lengths and the two boundary conditions discussed previously.

Figure 21 shows the thrust produced by the reference prismatic blade in cold (40°F) and hot (115°F) conditions at 18° collective pitch. Also shown on the figure is the thrust produced for blades with morphing sections extending from the root to 25% span, for both slit and continuous junction boundaries, at the same conditions. In the cold state, the morphing blade geometries closely resemble the reference prismatic blade, and therefore produce the same thrust of 21,000 lbs (depicted by the blue bar on Fig. 21). For the no-SMA blade, hot conditions result in a reduction in thrust to 18,410 lbs, resulting in a lost lift capability of 2,590 lbs. For the 25%-span morphing section with the continuous boundary, increase in camber in hot conditions results in a generated thrust of 18,620 lbs, representing a recovery of 210 lbs, or 8% of the lost lifting capability. For the slit boundary, the generated thrust increases further to 18,700 lbs, which represents a 290 lbs or 11% recovery of lost lifting capability.

Figure 22 illustrates the hover thrust and power requirement for the reference prismatic rotor (no-SMA) and the 25%-span morphing section with slit boundary, as a function of collective pitch. The solid lines depict the thrust and power of an uncambered rotor blade (both the reference prismatic blade as well as the morphing derivative) at 40°F. The two dashed lines represent the reference prismatic blade (no-SMA) and the camber morphing blade at 115°F. The camber morphing blade clearly offers a small but nonzero thrust benefit at a small but nonzero power penalty across all angles of attack. At 18° collective pitch, the rotor is close to stall and therefore further increase in collective cannot be used to generate additional thrust. This makes the SMA-induced camber an attractive alternative for lift recovery in hot conditions. On the other hand, the power requirement is within the available installed power on the Black Hawk helicopter.

Next, Figs. 23 and 24 consider a similar analysis for morphing sections extending from the root to 50% span. As before, the blue bar on Fig. 23 depicts the thrust produced in the cold state, and for the no-SMA blade hot conditions result in a reduction in thrust to 18,410 lbs, resulting in a lost lift capability of 2,590 lbs. For the 50%-span morphing section with the continuous boundary, increase in camber in hot conditions results in a generated thrust of 19,332 lbs, representing a recovery of 922 lbs, or 35% of the lost lifting capability. For the slit boundary, the generated thrust increases further to 19,547 lbs, which represents a 1,137 lbs or 43% recovery of lost lifting capability. Figure 24 illustrates the hover thrust and power requirement for the reference prismatic rotor (no-SMA) and the 50%-span morphing section with slit boundary, as a function of collective pitch. Again, the solid lines depict the thrust and power of an uncambered rotor blade at 40°F. The two dashed lines represent the reference prismatic blade (no-SMA) and the camber morphing blade at 115°F. The camber morphing blade now offers a moderate thrust benefit with an associated power cost. Additionally, in the hot environment, the SMA camber-morphing blade can provide a slightly greater maximum lift than the reference prismatic blade, which can be seen at collective values around 22-23°.

Finally, Figs. 25 and 26 present results for morphing sections extending from the blade root to 75% span. Again, the blue bar on Fig. 25 depicts the thrust produced in the cold state, and for the no-SMA blade hot conditions result in a reduction

in thrust to 18,410 lbs, resulting in a lost lift capability of 2,590 lbs. For the 75%-span morphing section with the continuous boundary, increase in camber in hot conditions results in a generated thrust of 20,416 lbs, representing a recovery of 2,006 lbs, or 76% of the lost lifting capability. For the slit boundary, the generated thrust increases further to 20,595 lbs, which represents a 2,185 lbs or 82% recovery of lost lifting capability. Figure 26 illustrates the hover thrust and power requirement for the reference prismatic rotor (no-SMA) and the 75%-span morphing section with slit boundary, as a function of collective pitch. Again, the solid lines depict the thrust and power of an uncambered rotor blade at 40°F. The two dashed lines represent the reference prismatic blade (no-SMA) and the camber morphing blade at 115°F. The camber morphing blade now offers a substantial thrust benefit with an associated power cost. At 115°F, the SMA camber-morphing blade can provide a much greater maximum lift than the reference prismatic blade, which can be seen at collective values between 20-23°.

CONCLUSION

The present study proposes and explores a new autonomous morphing concept, whereby an increase in helicopter rotor blade camber of the order of 12-13° is realized with increase in ambient temperature. The camber change is achieved through a proper integration of Shape Memory Alloys (SMAs) into the helicopter rotor blade. Some key observations from the study are presented below:

A slit junction between the morphing and non-morphing sections of the SMA camber-morphing blade induces a spanwise constant camber angle with temperature, while a continuous junction promotes spanwise variation.

In the slit configuration, the strain that the SMA undergoes to induce the camber change is primarily chordwise in nature. Whereas for the seamlessly integrated configuration, the strain is predominantly spanwise in the vicinity of the junction, but becomes partially chordwise at the inboard free end.

Incorporating the SMA camber-morphing skin along the inboard 25% span with a seamlessly integrated and a slit junction with the non-morphing section can recover 8% and 11% of the lift lost due to hot and high conditions (6000 ft, 115°F), respectively.

If the camber-morphing section is extended to 50% span, 35% and 43% of the lost lift can be recovered, respectively, with a moderate penalty in rotor power.

If the camber-morphing section is further extended to 75% span, 76% and 82% of the lost lift can be recovered, respectively, with an associated power penalty.

ACKNOWLEDGEMENT

For the duration of this research, Matthew DiPalma was supported by the Department of Defense through the National Defense Science & Engineering Graduate (NDSEG) Fellowship Program.

REFERENCES

1. Anusonti-Inthra, P., Sarjeant, R., Frecker, M., and Gandhi, F., "Design of a Conformable Rotor Airfoil Using Distributed Piezoelectric Actuators," AIAA Journal, Vol. 43, No. 8, Aug. 2005, pp. 1684–1695. doi:10.2514/1.1519.

2. Gandhi, F., Frecker, M., and Nissly, A., "Design Optimization of a Controllable Camber Rotor Airfoil," AIAA Journal, Vol. 46, No. 1, 2008, pp. 142–153. doi:10.2514/1.24476.

3. Grohmann, B., Maucher, C., and Prunhuber, T.et al., "Multidisciplinary Design and Optimization of Active Trailing Edge for Smart Helicopter Rotor Blade," Mechanics of Advanced Materials and Structures, Vol. 15, No. 3, 2008, pp. 307–324. doi:10.1080/15376490801907830.

4. Bilgen, O., Kochersberger, K. B., Inman, D. J., and Ohanian, O. J., III, "Macro-Fiber Composite Actuated Simply Supported Thin Airfoils," Smart Materials and Structures, Vol. 19, No. 5, 2010, Paper 055010. doi:10.1088/0964-1726/19/5/055010.

5. Bilgen,O., Kochersberger,K. B., Inman,D. J., and Ohanian,O. J., "Novel, Bidirectional, Variable Camber Airfoil via Macro-Fiber Composite Actuators," Journal of Aircraft, Vol. 47, No. 1, 2010, pp. 303–314. doi:10.2514/1.45452.

6. Bernhammer, L.O., Teeuwen, S. P.W., DeBreuker,R., van derVeen, G. J., and van Solingen, E., "Gust Load Alleviation of an Unmanned Aerial Vehicle Wing Using Variable Camber," Journal of Intelligent Material Systems and Structures, Vol. 25, No. 7, May 2014, pp. 795–805. doi:10.1177/1045389X13511010.

7. Woods, B. K. S., Friswell, M., and Wereley, N., "Advanced Kinematic Tailoring for Morphing Aircraft Actuation," AIAA Journal, Vol. 52, No. 4, April 2014, pp. 798–788. doi:10.2514/1.J052808.

8. Yokozeki, T., Sugiura, A., and Hirano, Y., "Development of Variable Camber Morphing Airfoil Using Corrugated Structure," Journal of Aircraft, Vol. 51, No. 3, 2014, pp. 1023–1029. doi:10.2514/1.C032573.

9. Strelec, J. K., Lagoudas, D. C., Khan, M. A., and Yen, J., "Design and Implementation of a Shape Memory Alloy Actuated Reconfigurable Airfoil," Journal of Intelligent Material Systems and Structures,Vol. 14, Nos. 4–5, 2003, p. 257–273. doi:10.1177/1045389X03034687.

10. Barbarino, S., Pecora, R., Lecce, L., Concilio, A., Ameduri, S., and De Rosa, L., "Airfoil Structural Morphing Based on S.M.A. Actuator Series: Numerical and Experimental Studies," Journal of Intelligent Material Systems and Structures, Vol. 22, No. 10, July 2011, pp. 987–1004. doi:10.1177/1045389X11416032.

11. Pecora, R., Barbarino, S., Concilio, A., Lecce, L., and Russo, S., "Design and Functional Test of a Morphing High Lift Device for a Regional Aircraft," Journal of Intelligent Material Systems and Structures, Vol. 22, No. 10, July 2011, pp. 1005–1023. doi:10.1177/1045389X11414083.

12. Ameduri, S., Brindisi, A., Tiseo, B., Concilio, A., and Pecora, R., "Optimization and Integration of Shape Memory Alloy (SMA)-Based Elastic Actuators Within a Morphing Flap Architecture," Journal of Intelligent Material Systems and Structures, Vol. 23, No. 4, March 2012, pp. 381–396. doi:10.1177/1045389X11428672.

13. Bil, C., Massey, K., and Ermira, J. A., "Wing Morphing Control with Shape Memory Alloy Actuators," Journal of Intelligent Material Systems and Structures, Vol. 24, No. 7, May 2013, pp. 879–898. doi:10.1177/1045389X12471866.

14. Prabhakar, T., Gandhi, F., and McLaughlin, D., "A Centrifugal Force Actuated Variable Span Morphing Helicopter Rotor," *63rd Annual AHS International Forum and Technology Display*, Virginia Beach, VA, May 1-3, 2007.

15. Misiorowski, M., Pontecorvo, M., and Gandhi, F., "A Bi-Stable System for Rotor Span Extension in Rotary-Wing Micro Aerial Vehicles," 23rd AIAA/ASME/AHS Adaptive Structures Conference, AIAA Science and Technology Forum 2015, Jan 5-9, 2015, Kissimmee, Florida.

16. Moser, P., Barbarino, S., and Gandhi, F., "Helicopter Rotor Blade Chord Extension Morphing using a Centrifugally Actuated von-Mises Truss," *Journal of Aircraft*, Vol. 51, No. 5 (2014), pp. 1422-1431. doi: 10.2514/1.C032299.

17. Lake, R. C., Nixon, M. W., Wilbur, M. L., Singleton, J. D., and Mirick, P. H. "A demonstration of passive blade twist control using extension-twist coupling", 33rd Structures, Structural Dynamics and Materials Conference, Structures, Structural Dynamics, and Materials and Co-located Conferences, 1992. doi:10.2514/6.1992-2468.

18. Nampy, S. and Smith, E., "Design Evaluation of Model and Full-scale Flexible Matrix Composites Tiltrotor Blades with Extension-twist Coupling," AHS International 62nd Annual Forum, 2006. doi:10.1177/1045389X10369719.

19. Ward, E. A., Chopra, I., and Datta, A., "Design of Self-Twisting Rotor Blades for High-Speed Compound Rotorcraft," 25th AIAA/AHS Adaptive Structures Conference, 2017. doi:10.2514/6.2017-0292.

20. Ward, E. A., Chopra, I., and Datta, A., "RPM Driven Extension-Torsion Coupled Self-Twisting Rotor Blades," AHS International 73rd Annual Forum and Technology Display, 2017.

21. DiPalma, M., Ferede, E., and Gandhi, F., "Optimization of Extension-Twist Coupled Composite Blades for High-Speed Rotorcraft," *Proceedings of the 74th American Helicopter Society Annual Forum*, Phoenix, Arizona, May 15-17, 2018.

22. Auricchio, F., and R.L. Taylor, "Shape-Memory Alloys: Modeling and Numerical Simulations of the Finite-Strain Superelastic Behavior," Computer Methods in Applied Mechanics and Engineering, vol. 143, pp. 175–194, 1996.

23. Lagoudas, D., "Shape Memory Alloys: Modeling and Engineering Applications," Springer Science & Business Media, New York, NY, 2008.

24. Saberai, H., Khoshlahjeh, M., Ormiston, R., and Rutkowski, M. "Overview of RCAS and Application to Advanced Rotorcraft Problems," AHS 4thDecennial Specialists'Conference on Aeromechanics, San Francisco, CA, Jan. 21-23, 2004.

TABLES AND FIGURES

Table 1 – Material properties for the other components

Component	Material	E	ν	ρ
Blade Core	Isotropic Elastomer	180 MPa	0.3	1410 kg/m^3
Blade Skin	Symmetric Composite Layup	100 MPa	0.45	2000 kg/m^3
Trailing Edge	Aluminum 2024	72 GPa	0.3	2700 kg/m^3

Table 2 – Material properties for the SMA sheet

E_A (GPa)	E_M (GPa)	ν_A	ν_M	ε_L	C^M (MPa)	C^A (MPa)	T_{ref} (K)	σ^{MF} (MPa)	σ^{MS} (MPa)	σ^{AS} (MPa)	σ^{AF} (MPa)
72	40	0.33	0.33	0.05	8	8	311	364	224	196	56

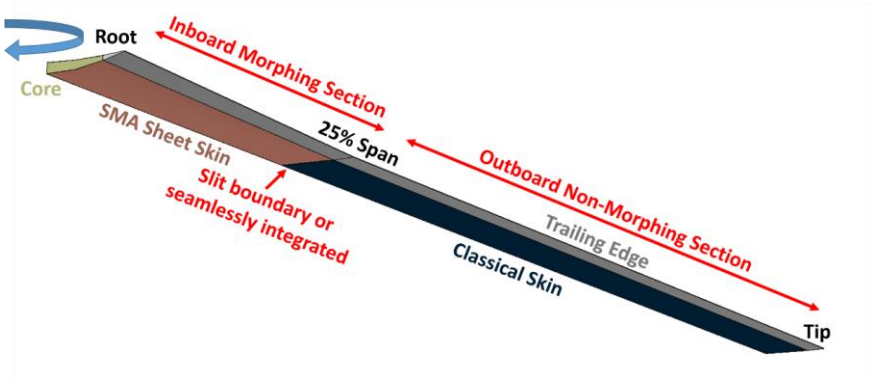

Figure 1 – View of the underside of the blade aft of the leading edge spar

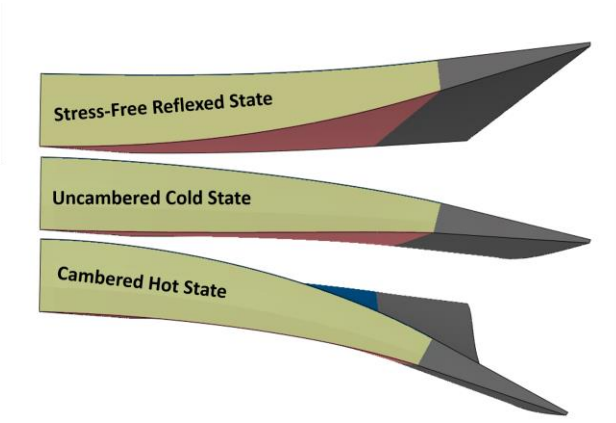

Figure 2 – View down the blade length (from the blade root) depicting the stress-free reflexed, cold, and hot states

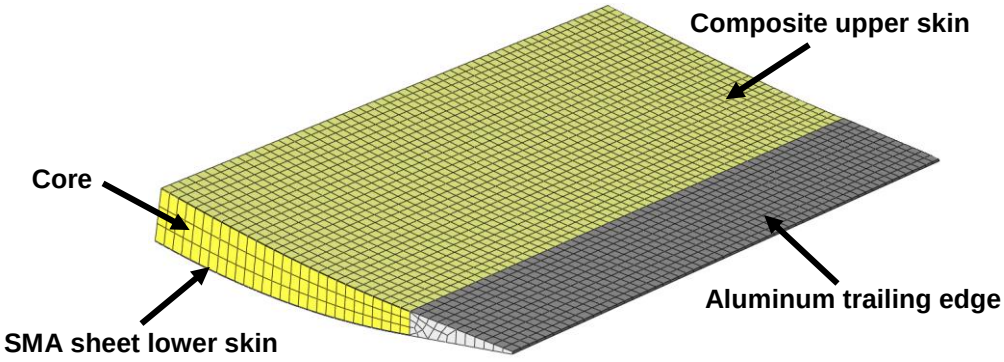

Figure 3 – Sample of finite element mesh used in structural analysis

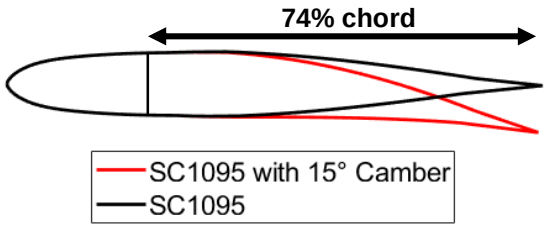

Figure 4 – Geometry of baseline SC1095 airfoil and 15° cambered derivative

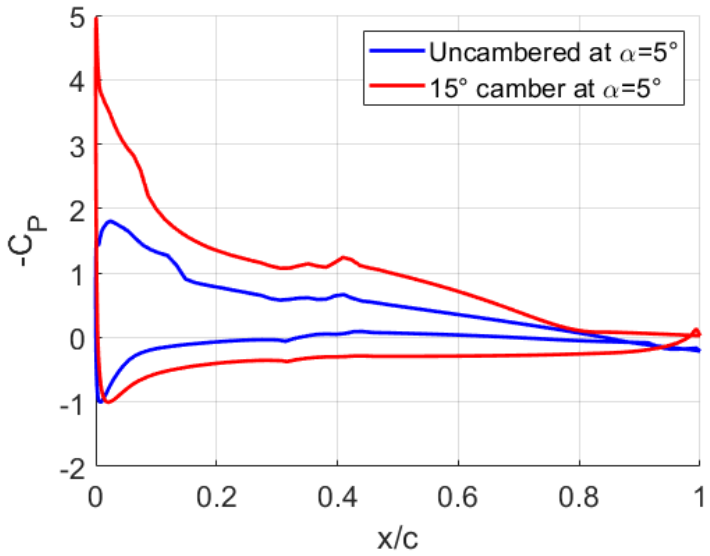

Figure 5 – Chordwise C_P comparison between baseline SC1095 and 15° cambered derivative at α=5°

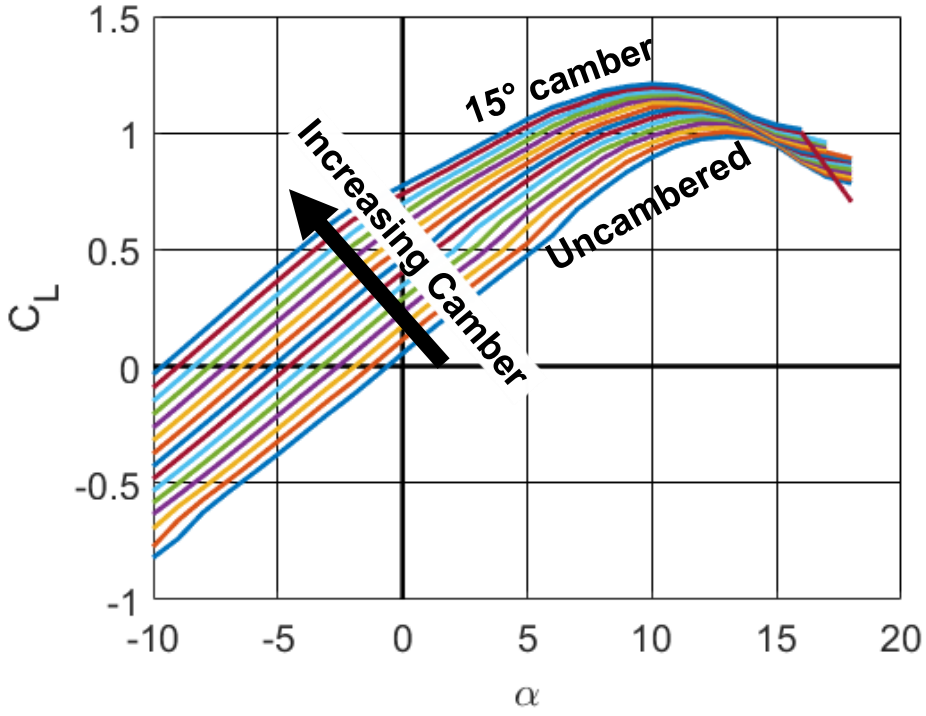

Figure 6 – C_L vs. α for increasing camber on SC1095 airfoil

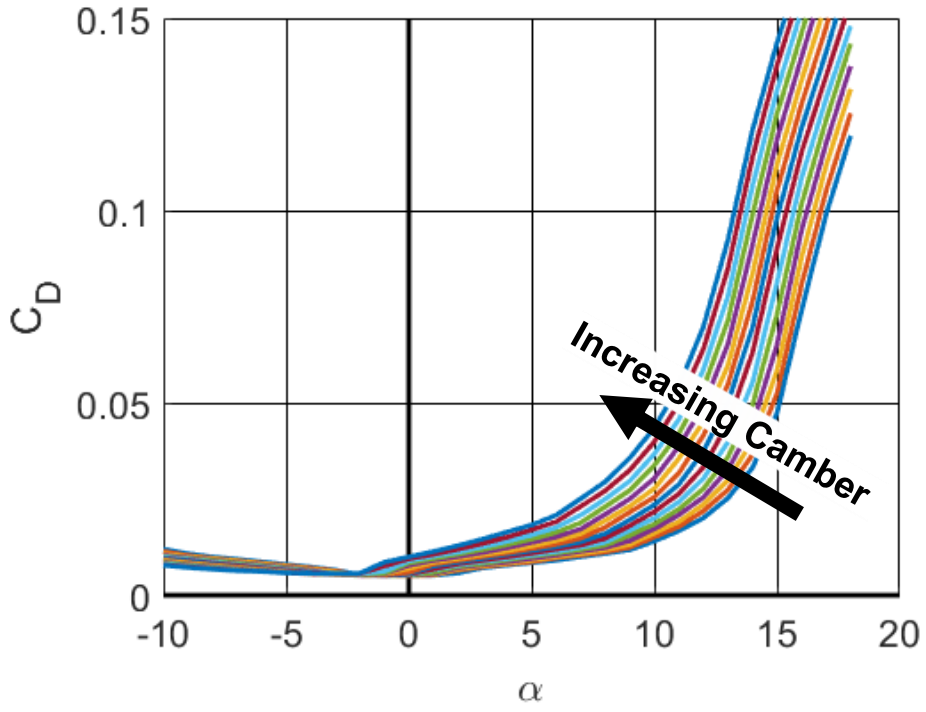

Figure 7 – C_D vs. α for increasing camber on SC1095 airfoil

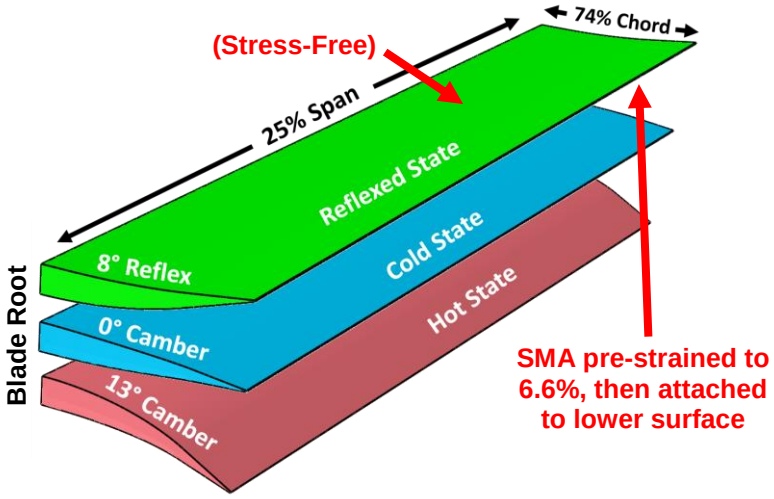

Figure 8 – Stress-free, low-temperature and high-temperature states with a slit between morphing and non-morphing sections

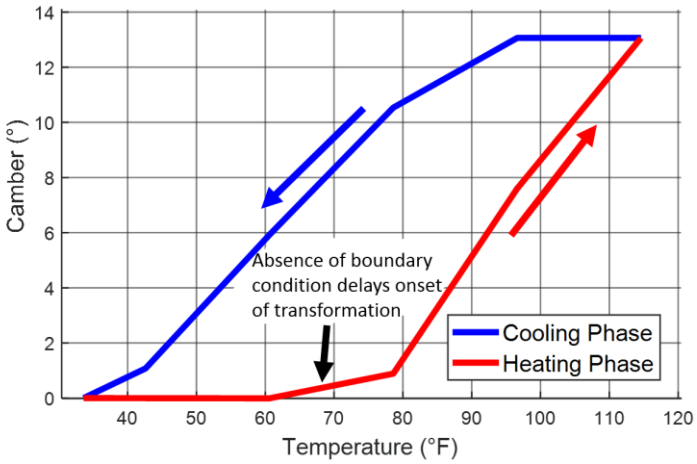

Figure 9 – Camber versus temperature with a slit between morphing and non-morphing sections

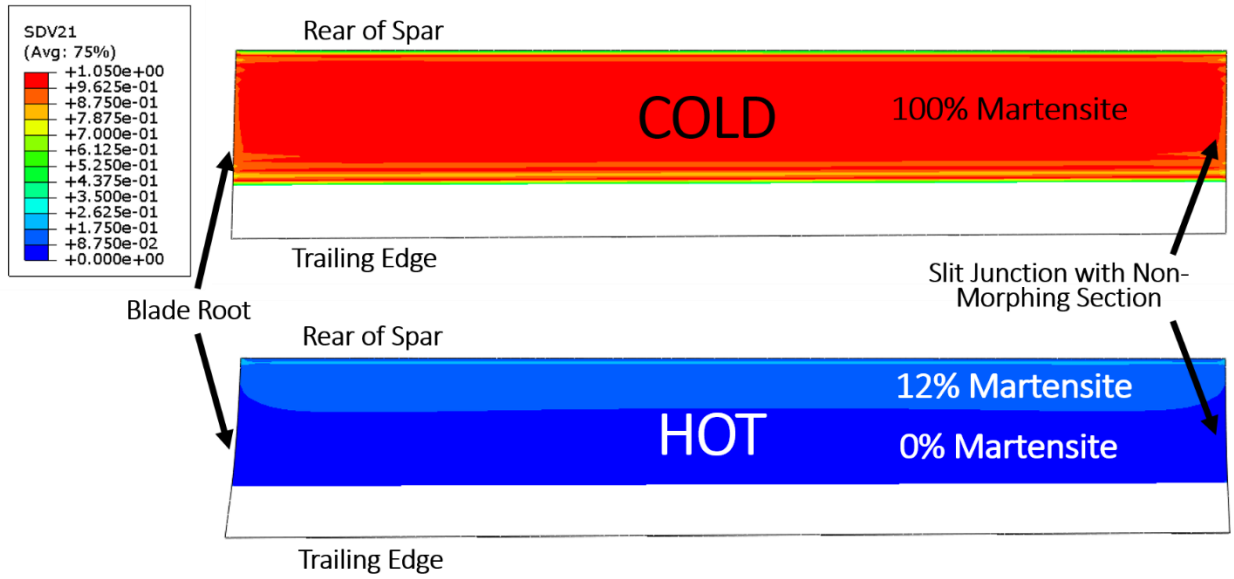

Figure 10 – Martensite volume fraction in the SMA along lower surface (viewed from above with top skin and core removed) for 25%-span morphing section with slit junction.

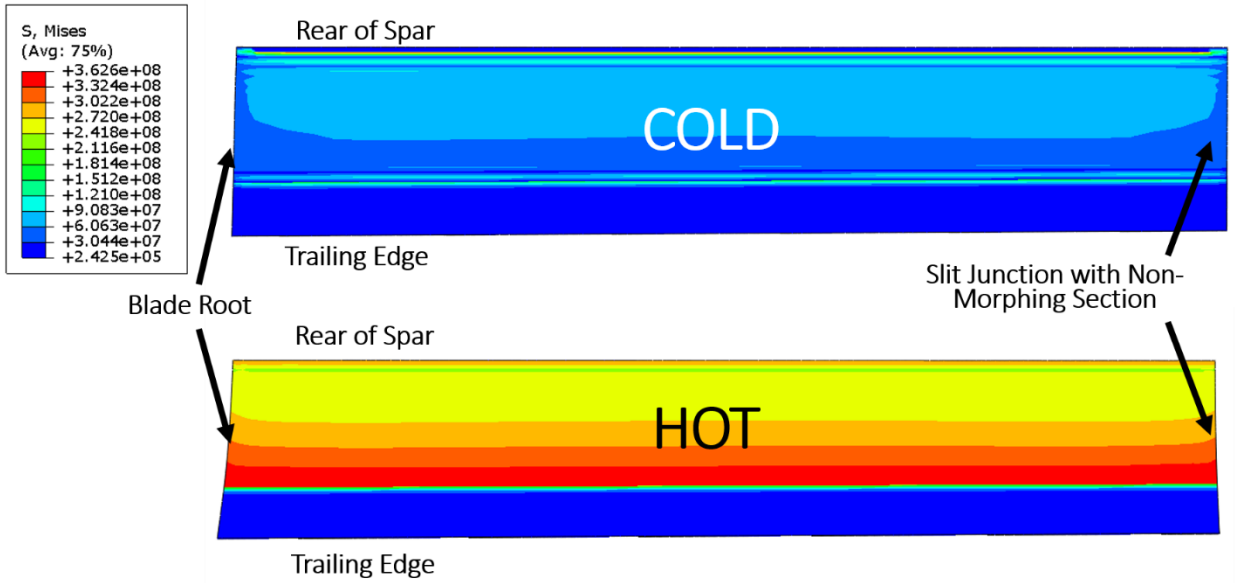

Figure 11 – Von Mises stress in the SMA along lower surface (viewed from above with top skin and core removed) for 25%-span morphing section with slit junction.

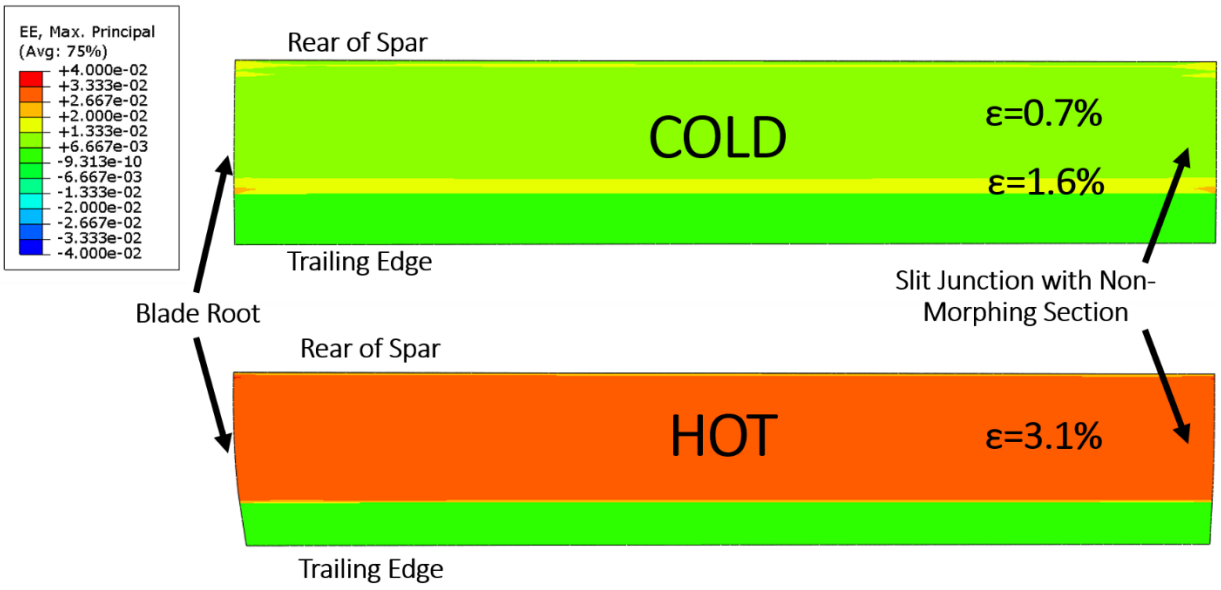

Figure 12 – Maximum chordwise strain along upper surface (viewed from above) for 25%-span morphing section with slit junction.

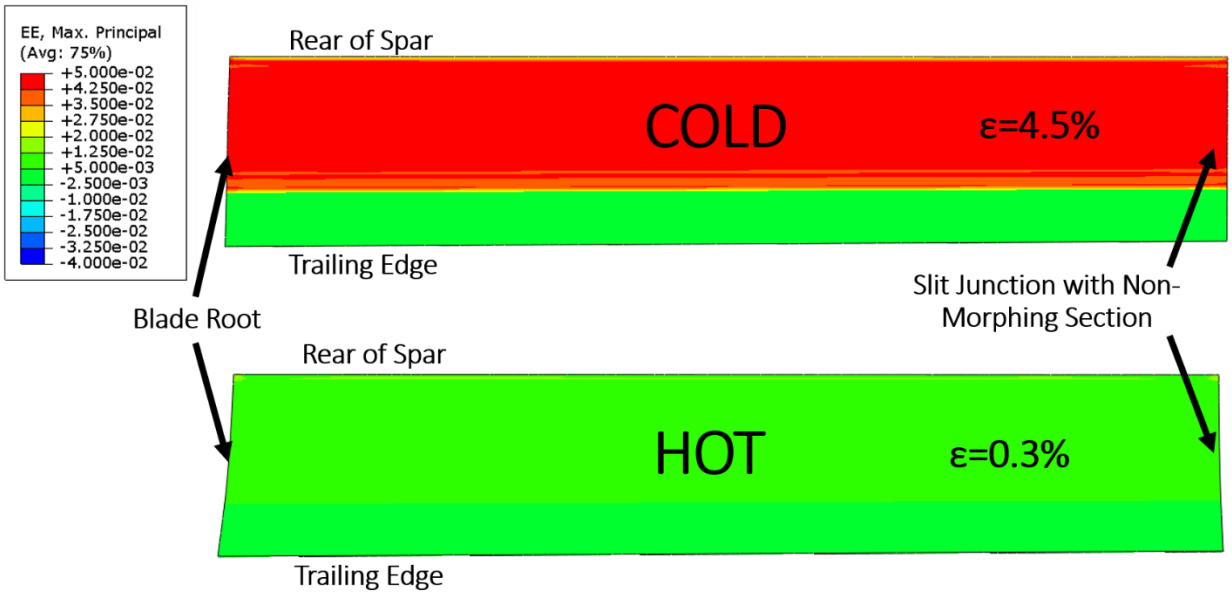

Figure 13 – Maximum chordwise strain in the SMA along lower surface (viewed from above with top skin and core removed) for 25%-span morphing section with slit junction.

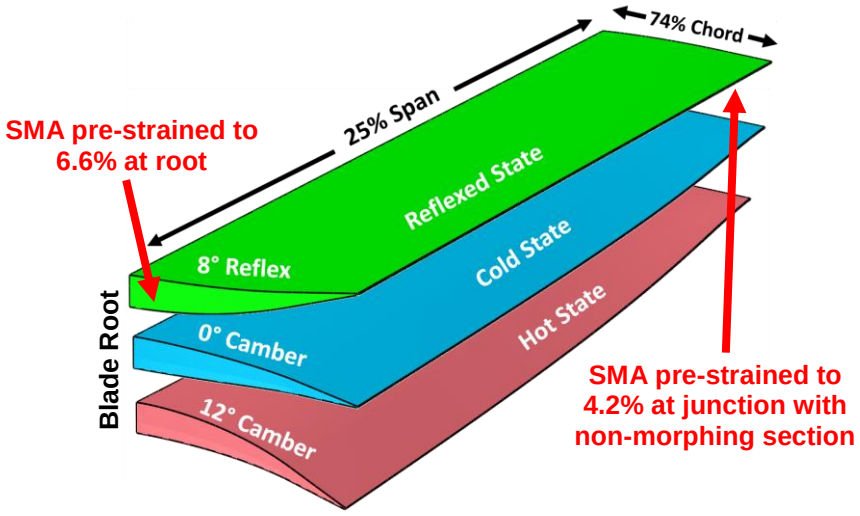

Figure 14 – Stress-free, low-temperature, and high temperature states for seamlessly integrated morphing section

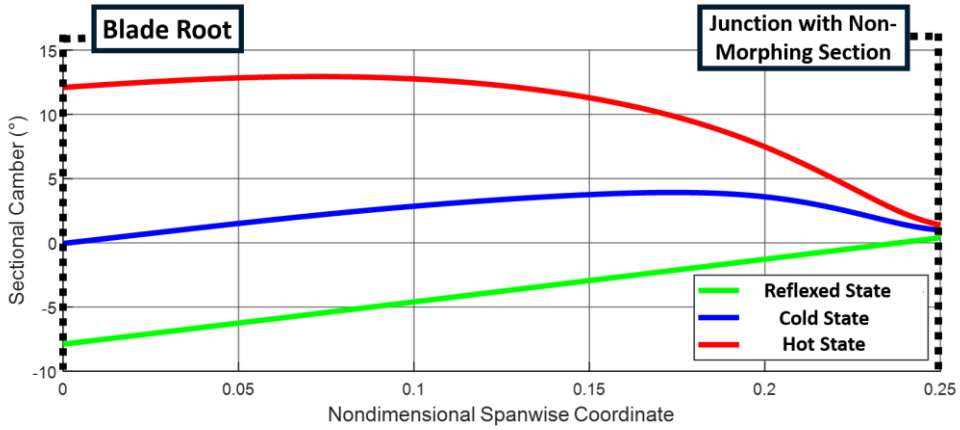

Figure 15 – Inboard camber distribution for the seamlessly integrated morphing section

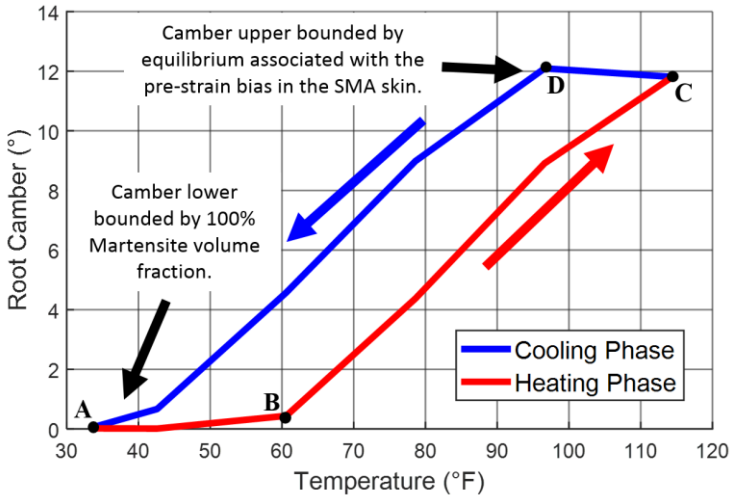

Figure 16 – Root camber versus temperature for the seamlessly integrated morphing region

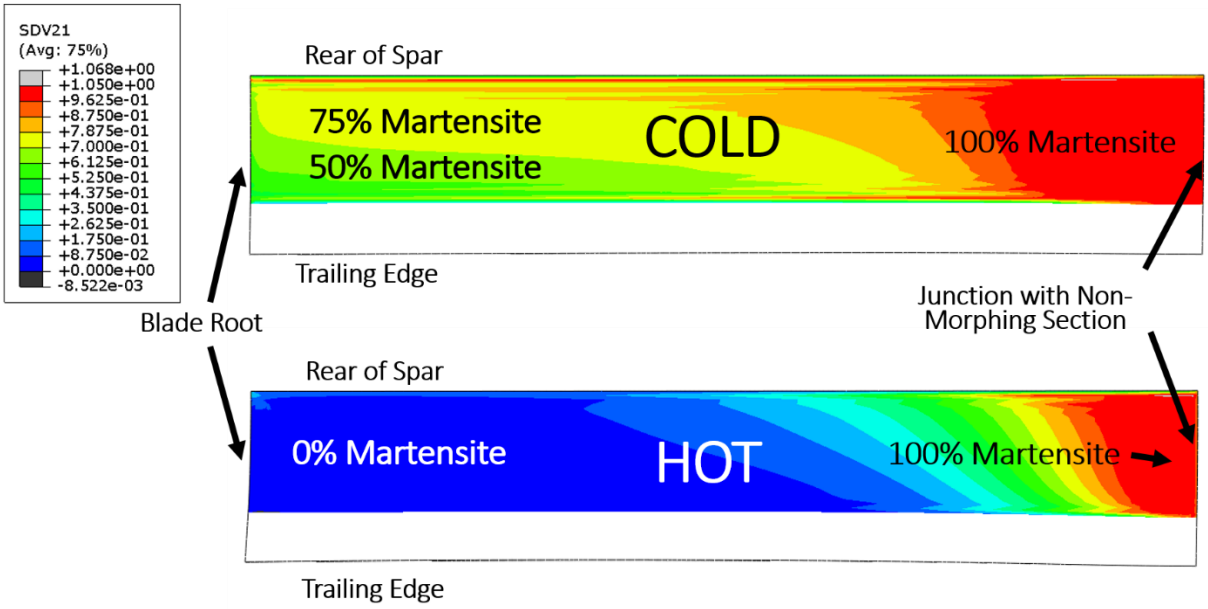

Figure 17 – Martensite volume fraction in the SMA along lower surface (viewed from above with top skin and core removed) for 25%-span morphing section with continuous junction.

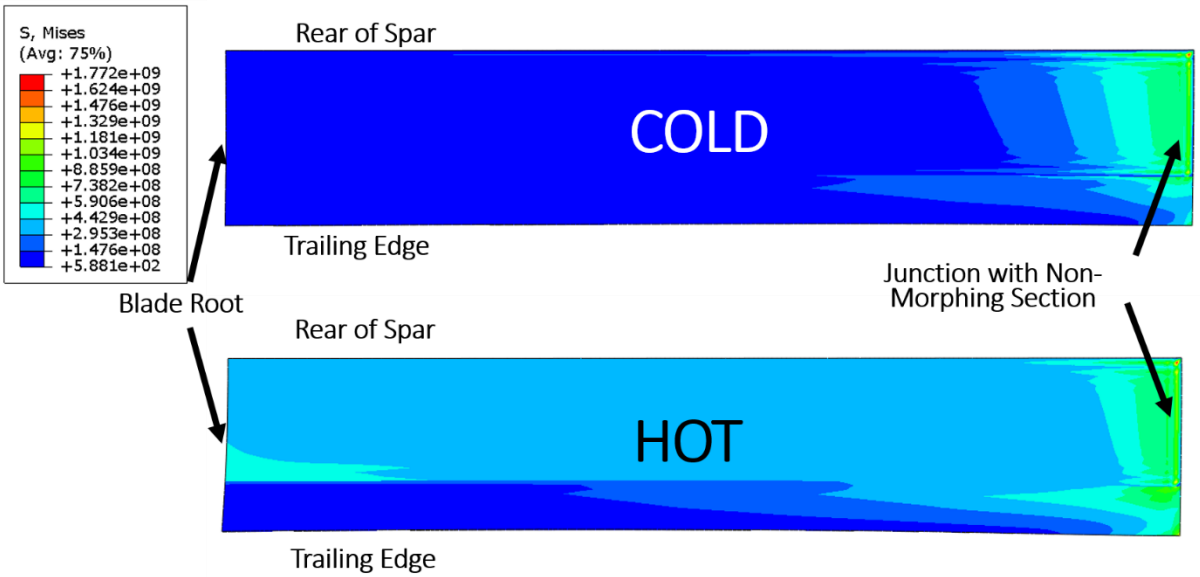

Figure 18 – Von Mises stress in the SMA along lower surface (viewed from above with top skin and core removed) for 25%-span morphing section with continuous junction.

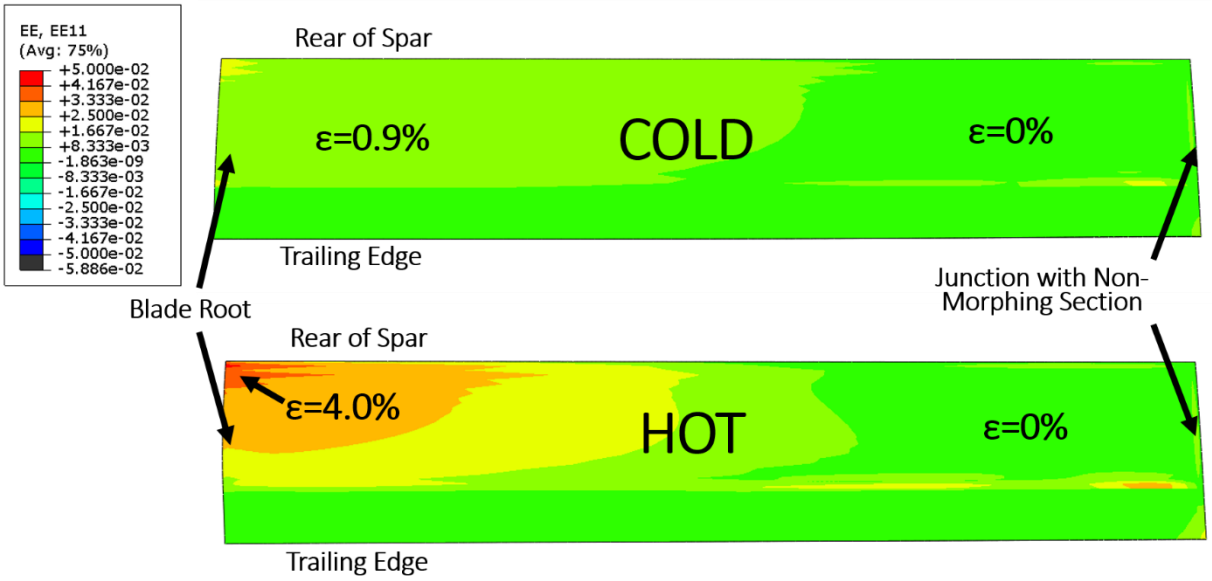

Figure 19 – Maximum in-plane principle strain along upper surface (viewed from above) for 25%-span morphing section with continuous junction.

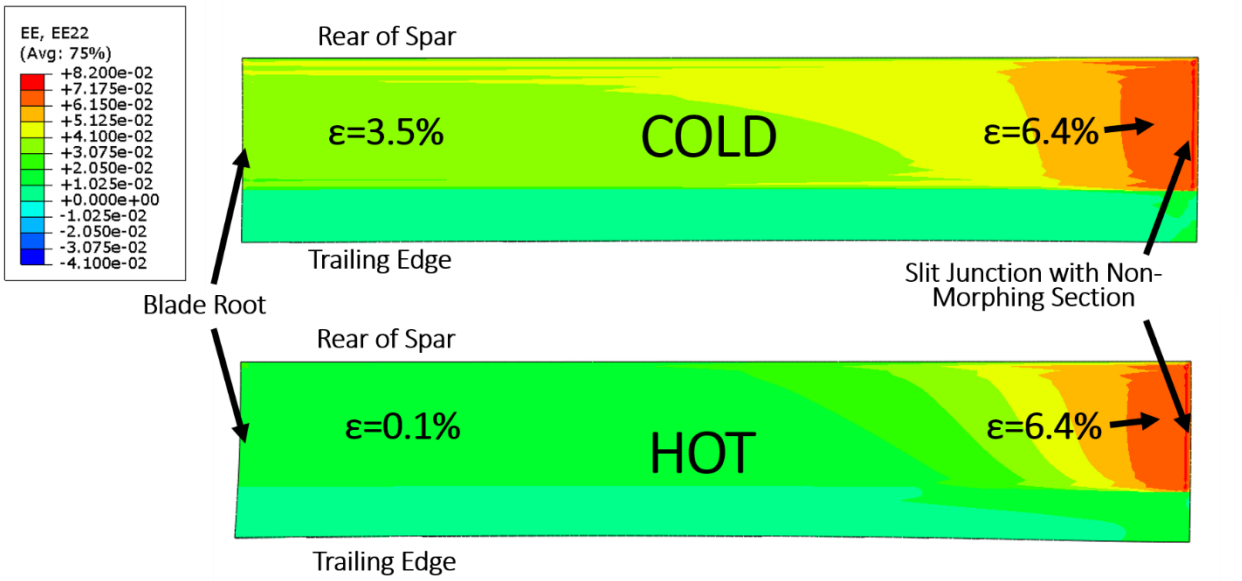

Figure 20 – Maximum in-plane principle strain in the SMA along lower surface (viewed from above with top skin and core removed) for 25%-span morphing section with continuous junction.

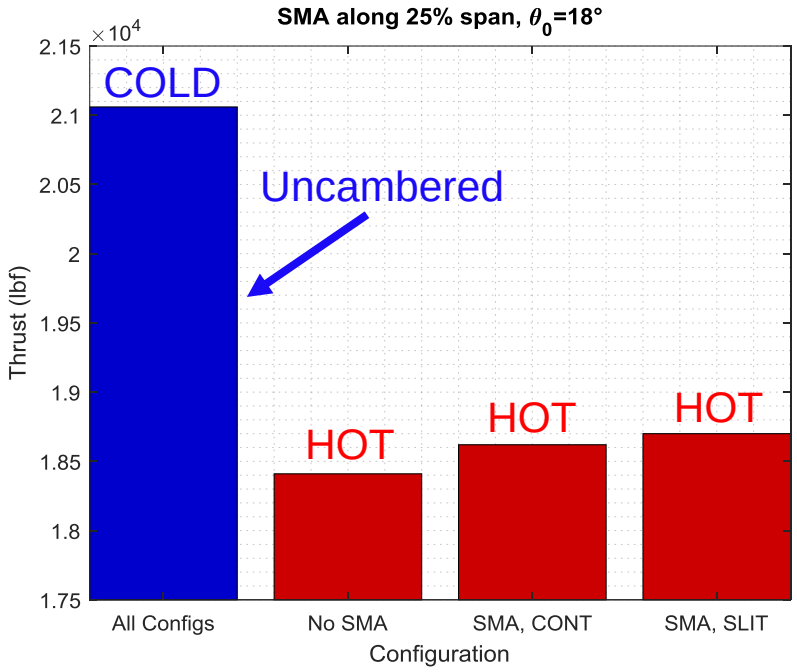

Figure 21 – Thrust in Cold (blue) and Hot (red) environments for a prismatic blade, camber-morphing blade with continuous junction, and camber-morphing blade with slit junction along 25% span

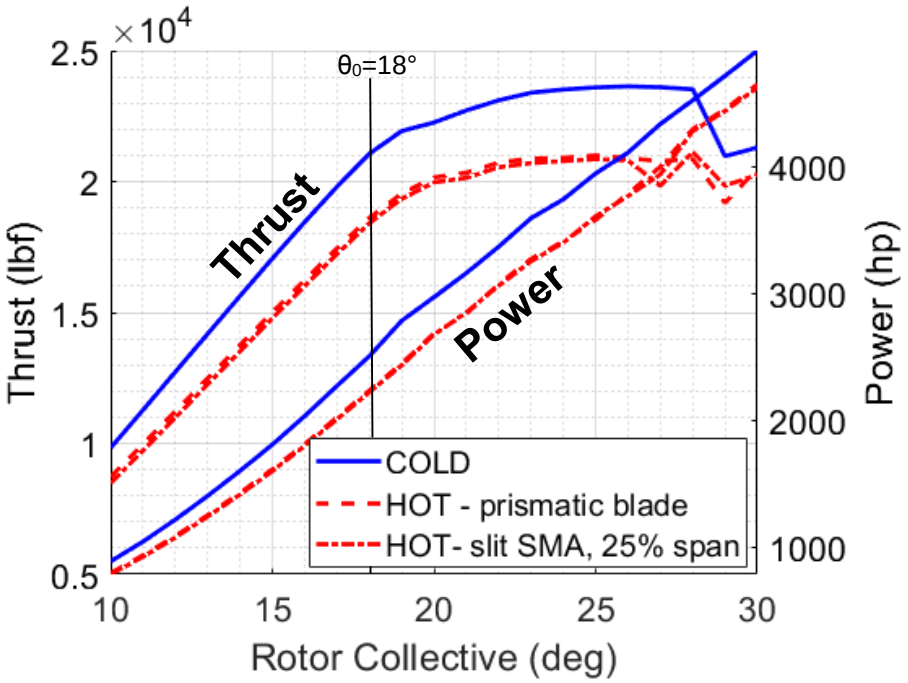

Figure 22 – Thrust and power for hovering slit 25%-span camber morphing blade, compared against prismatic UH-60A Black Hawk blade in hot and cold environments.

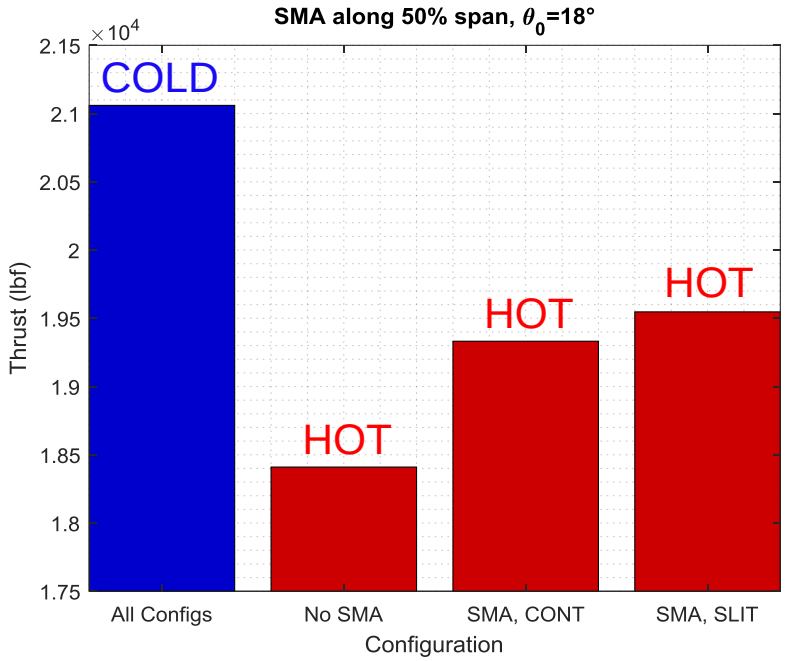

Figure 23 – Thrust in Cold (blue) and Hot (red) environments for a prismatic blade, camber-morphing blade with continuous junction, and camber-morphing blade with slit junction along 50% span

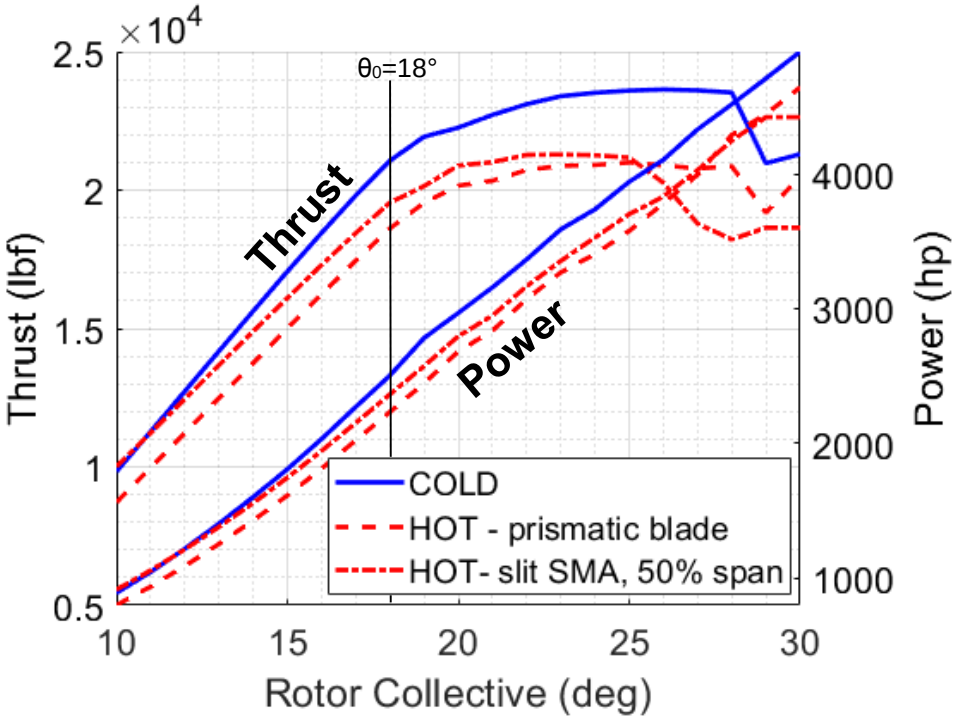

Figure 24 – Thrust and power for hovering slit 50%-span camber morphing blade, compared against prismatic UH-60A Black Hawk blade in hot and cold environments.

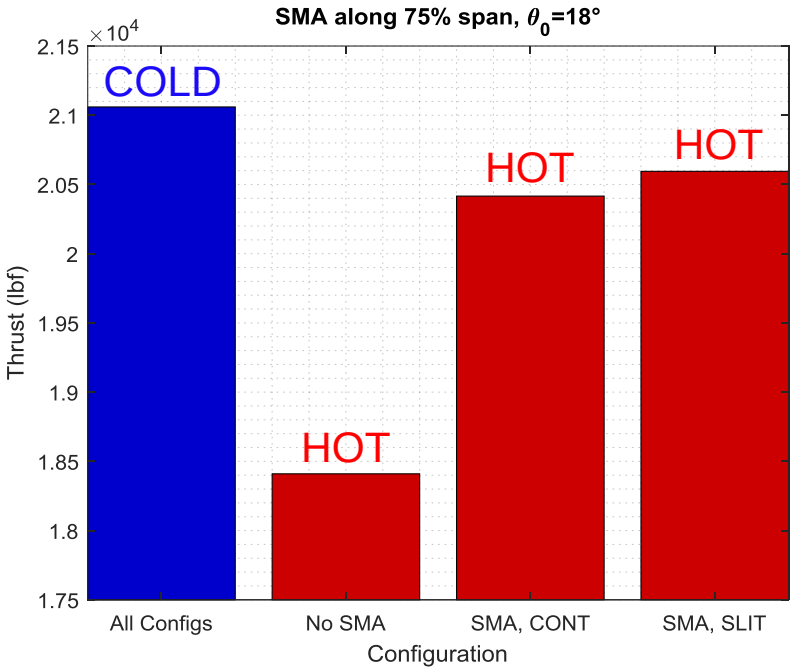

Figure 25 – Thrust in Cold (blue) and Hot (red) environments for a prismatic blade, camber-morphing blade with continuous junction, and camber-morphing blade with slit junction along 75% span

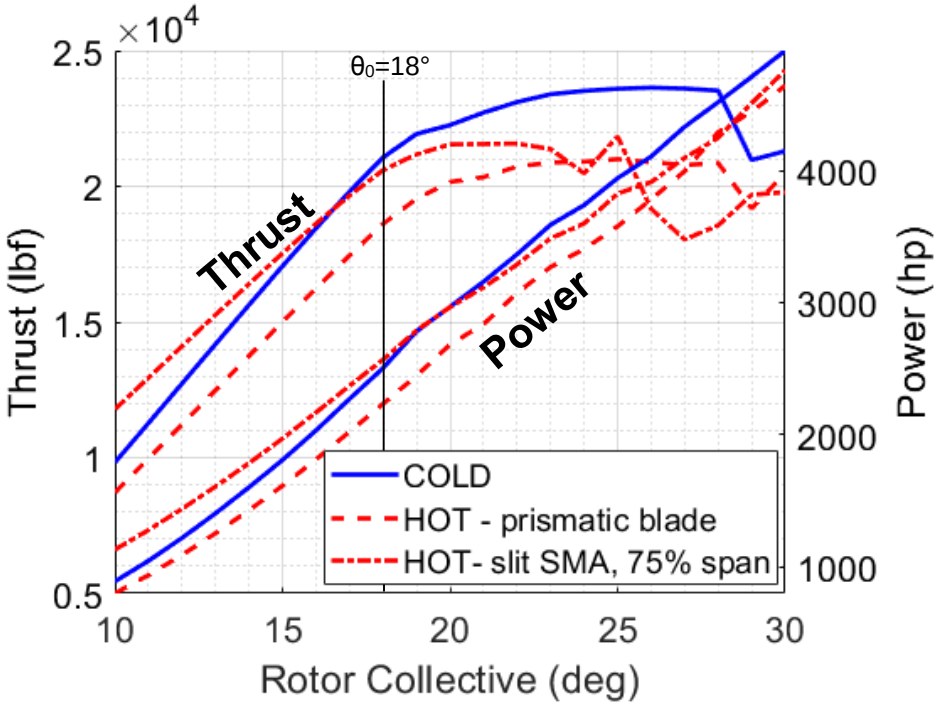

Figure 26 – Thrust and power for hovering slit 75%-span camber morphing blade, compared against prismatic UH-60A Black Hawk blade in hot and cold environments.